PAPER • OPEN ACCESS

Unveiling V modes: enhancing CMB sensitivity to BSM physics with a non-ideal half-wave plate

To cite this article: N. Raffuzzi *et al* JCAP03(2025)009

View the article online for updates and enhancements.

Unveiling V modes: enhancing CMB sensitivity to BSM physics with a non-ideal half-wave plate

N. Raffuzzi [a,b] **M. Lembo** [a,b] **S. Giardiello** [c,a] **M. Gerbino** [b] **M. Lattanzi** [b]
P. Natoli [a,b] **and L. Pagano** [a,b,d]

[a] *Dipartimento di Fisica e Scienze della Terra, Università degli Studi di Ferrara,*
via Saragat 1, I-44122 Ferrara, Italy

[b] *Istituto Nazionale di Fisica Nucleare, Sezione di Ferrara,*
via Saragat 1, I-44122 Ferrara, Italy

[c] *School of Physics and Astronomy, Cardiff University,*
The Parade, Cardiff, Wales CF24 3AA, U.K.

[d] *Institut d'Astrophysique Spatiale, CNRS, Univ. Paris-Sud, Université Paris-Saclay,*
Bât. 121, 91405 Orsay cedex, France

E-mail: nicolelia.raffuzzi@unife.it, margherita.lembo@unife.it,
GiardielloS@cardiff.ac.uk, gerbinom@fe.infn.it, lattanzi@fe.infn.it,
ntlpla@unife.it, pgnlcu@unife.it

ABSTRACT: V-mode polarization of the cosmic microwave background is expected to be vanishingly small in the ΛCDM model and, hence, usually ignored. Nonetheless, several astrophysical effects, as well as beyond standard model physics could produce it at a detectable level. A realistic half-wave plate — an optical element commonly used in CMB experiments to modulate the polarized signal — can provide sensitivity to V modes without significantly spoiling that to linear polarization. We assess this sensitivity for some new-generation CMB experiments, such as the LiteBIRD satellite, the ground-based Simons Observatory and a CMB-S4-like experiment. We forecast the efficiency of these experiments to constrain the phenomenology of certain classes of BSM models inducing mixing of linear polarization states and generation of V modes in the CMB. We find that new-generation experiments can improve current limits by 1-to-3 orders of magnitude, depending on the data combination. The inclusion of V-mode information dramatically boosts the sensitivity to these BSM models.

Contents

1 Introduction

Observations of anisotropies in the cosmic microwave background (CMB) radiation proved a major observational channel for modern cosmology. The Planck satellite observed them in temperature and polarization with unprecedented precision, providing state-of-the-art constraints on cosmology and fundamental physics [1]. Ground-based experiments have complemented these observations, especially targeting the polarization signal [2–5]. CMB E-mode polarization remains a key focus for next-generation experiments, aiming to achieve a cosmic-variance-limited estimate of the optical depth to reionization τ [6], the least constrained parameter in the ΛCDM model. Also, observations of large-scale B-mode polarization are crucial for improving sensitivity to, or detecting, the tensor-to-scalar ratio r [6–8], ac proxy for primordial gravitational waves. Enhanced sensitivity to small-scale E-mode and B-mode anisotropies will further constrain parameters of ΛCDM and its extensions [7, 8]. Additionally, improved observations of polarized CMB will help explore BSM physics, such as deviations from standard electromagnetism [9], neutrino properties [6], dark sectors [10], and supersymmetries [11, 12].

The circular polarization of the CMB, or V modes,[1] is expected to be small in the standard cosmological model, as it is not produced by Thomson scattering during recombination and reionization. Several standard and non-standard physical mechanism can however source a degree of circular polarization in CMB photons, by converting linear polarization

---

[1]The terms E and B modes refer to distinct geometrical patterns corresponding to curl-less (E) and divergence-less (B) components of the linear polarization field on the sky [13]. Unlike E and B, V polarization does not correspond to geometrical patterns such as gradients or curls, but represents instead the handedness of polarization. [14, 15]. However, we will loosely use the term "V-modes" to refer to circular polarization. Circular polarization involves the wave's rotational symmetry rather than its orientation in the plane perpendicular to the line of sight.

generated at the last scattering surface. Among the standard mechanisms, photon-photon scattering via Heisenberg-Euler interaction at recombination produces the strongest circular polarization [16, 17]. For a comprehensive overview of conventional mechanisms that can source V-mode polarization in the CMB radiation see e.g. ref. [15]. In the realm of non-standard physics, extensions of QED suggest that V-modes arise in the presence of Lorentz-violating operators [9, 18, 19]. Additionally, refs. [20, 21] show that a pseudo-scalar field or axion inflation leads to V-mode generation. Magneto-optic effects are another class of phenomena capable of generating CMB circular polarization [22, 23]. The detection of circular polarization in the CMB has therefore the potential to offer further evidence for novel physics or more stringent constraints than those available from observations of linear polarization only.

Vast improvements are expected in the observation of the CMB polarized signal both from ground-based experiments, such as the currently running Simons Observatory (SO) [7] and the next-generation CMB experiment CMB-S4 [8], and from satellites such as the LiteBIRD mission [6]. Achieving the promised sensitivity to detect the faint cosmological signals hidden in polarization requires monitoring and minimizing systematic effects. Upcoming observations will benefit from improved scanning strategies, including the use of a rotating half-wave plate (HWP) as a polarization modulator for SO and LiteBIRD. Previous studies have already demonstrated the effectiveness of a rotating HWP in mitigating 1/f noise, [24], and reducing temperature-to-polarization leakage resulting from pair-differencing of orthogonal detectors [25, 26]. However, despite the addition of a HWP is remarkably useful, the inclusion of another optical element in the acquisition chain brings along additional systematic effects, which in turn may compromise the final scientific product. One example is a HWP with a non-ideal phase shift, i.e., a HWP inducing a phase difference $\neq 180°$ between the two components of the electromagnetic wave traversing it. Interestingly enough, this deviation, possibly degrading the sensitivity to linear polarization, can also cause a coupling between total intensity and circular polarization. This would allow to investigate the presence of V modes in the CMB radiation [27]. In this paper, we exploit this possibility showing how forthcoming CMB experiments, equipped with HWPs, can be sensitive to circular polarization and, in turn, provide valuable information on a specific class of BSM physical models. We investigate a simple mechanism named the Generalized Faraday Effect (GFE), i.e. the mixing of CMB polarization states, including a partial conversion of linear into circular polarization [28, 29].

The paper is structured as follows: section 2 introduces the mathematical formalism (Jones calculus [30]) describing the optical behaviour of a (realistic) HWP, the instrumental systematic effect induced by a non-ideal phase shift, as well as the expected sensitivity to V modes; section 3 illustrates the specific mechanism generating circular polarization and its cosmological phenomenology, while section 4 describes the analysis method adopted in this work; in section 5, we present the results of the analysis, forecasting the performance of future CMB experiments. Finally, section 6 provides conclusions. Appendix A includes a full set of plots with posterior probability distributions of the key cosmological parameters for this work and for each experiment configuration considered in this analysis.

2 Sensitivity to V modes

In this section, we give an overview of the mathematical framework to model a HWP with non-ideal phase shift β (for a detailed description, see, e.g., [31, 32]). We also provide an estimate of the sensitivity to V modes for a generic CMB experiment employing a non-ideal HWP.

2.1 The non-ideal HWP

An ideal half-wave plate (HWP) is an optical device that induces a π-phase shift between the two orthogonal components of the incident wave. In the Jones formalism, the matrix describing the behavior of an ideal HWP is:

$$\mathbf{J}_{\text{HWP}}^{\text{Ideal}} = \begin{pmatrix} 1 & 0 \\ 0 & -1 \end{pmatrix}.$$

A realistic HWP can be described by the more general Jones matrix [31]:

$$\mathbf{J}_{\text{HWP}} = \begin{pmatrix} 1 + h_1 & \zeta_1 e^{i\chi_1} \\ \zeta_2 e^{i\chi_2} & -(1 + h_2)e^{i\beta} \end{pmatrix}, \tag{2.1}$$

where all but one entries of the matrix (e.g., J_{11}) are complex. The parameters $h_{1,2}$ are real and negative-defined, and indicate deviations from unitary transmission of the two polarized components, $E_{x,y}$, of the incident light due to absorption and reflection. The parameters $\zeta_{1,2}$ and $\chi_{1,2}$ correspond to the amplitudes and phases of the off-diagonal terms that are responsible for cross-polarization, i.e., mixing between the two orthogonal components of the wave. The parameter β represents the departure from the ideal phase shift of π. In this work, we focus on the effects of a non-vanishing β and how it can be used to measure circular polarization. In the following, we assume for simplicity that the effects due to absorption and cross-polarization are negligible and fix the relative parameters in eq. (2.1) to zero. The Jones matrix of a HWP with non-ideal phase shift and spinning with angular velocity ω is:

$$\mathbf{J}_{\text{HWP}}(\theta) = \mathbf{R}^{\text{T}}(\theta)\mathbf{J}_{\text{HWP}}\mathbf{R}(\theta) = \begin{pmatrix} J_{11}(\theta) & J_{12}(\theta) \\ J_{21}(\theta) & J_{22}(\theta) \end{pmatrix}, \quad \text{with} \quad \mathbf{R}(\theta) = \begin{pmatrix} \cos\theta & \sin\theta \\ -\sin\theta & \cos\theta \end{pmatrix}, \tag{2.2}$$

where $\theta = \omega t$ is the time-dependent angle between the HWP fast axis and the x-axis in the chosen reference frame, and:

$$\begin{aligned} J_{11}(\theta) &= \cos^2\theta - e^{i\beta}\sin^2\theta \\ J_{12}(\theta) &= J_{21}(\theta) = \left(1 + e^{i\beta}\right)\cos\theta\sin\theta \\ J_{22}(\theta) &= -e^{i\beta}\cos^2\theta + \sin^2\theta. \end{aligned} \tag{2.3}$$

In the case under study, the complete optical chain traversed by the incoming signal includes a rotating HWP, two orthogonal polarizers, and the detector. Eventually, the Jones matrix of the full optical chain[2] is:

$$\mathbf{J}_{x,y}(\theta) = \mathbf{J}_{\text{pol},(x,y)}\mathbf{R}^T(\theta)\mathbf{J}_{\text{HWP}}\mathbf{R}(\theta), \quad \text{with} \quad \mathbf{J}_{\text{pol,x}} = \begin{pmatrix} 1 & 0 \\ 0 & 0 \end{pmatrix}, \quad \mathbf{J}_{\text{pol,y}} = \begin{pmatrix} 0 & 0 \\ 0 & 1 \end{pmatrix}. \tag{2.4}$$

---

[2]Note that this optical chain does not include information about the instrument orientation. The primary goal of this analysis is not to define an explicit scanning strategy, but rather to establish the polarimeter's efficiency through variations in the HWP phase-shift. See [32] for details.

So far, we have considered a scenario where the incoming wave is fully polarized and has a quasi-monochromatic frequency. However, the CMB signal is only partially polarized, and a CMB experiment measures the time-averaged incident intensity. Therefore, it is more natural to express the signal in terms of the Stokes vector $s = (T, Q, U, V)$, and employ the Müller formalism [33], which also simplifies tracking the impact on each Stokes parameter.

Given a Jones matrix, it is straightforward to compute the corresponding 4×4 Müller matrix. Explicitly, the Müller elements, for the x-oriented polarizer, are:

$$
\begin{aligned}
\mathbf{M}^x_{TT} &= \frac{1}{2}\left(|\mathrm{J}_{11}|^2 + |\mathrm{J}_{12}|^2\right) = \frac{1}{2} \\
\mathbf{M}^x_{TQ} &= \frac{1}{2}\left(|\mathrm{J}_{11}|^2 - |\mathrm{J}_{12}|^2\right) = \frac{1}{2}\mathrm{Cos}\left(\frac{\beta}{2}\right)^2 \mathrm{Cos}(4\theta) \\
\mathbf{M}^x_{TU} &= \mathrm{Re}\left[(\mathrm{J}_{11}\mathrm{J}^*_{12})\right] = \frac{1}{2}\mathrm{Cos}\left(\frac{\beta}{2}\right)^2 \mathrm{Sin}(4\theta) \\
\mathbf{M}^x_{TV} &= \mathrm{Im}\left[(\mathrm{J}_{11}\mathrm{J}^*_{12})\right] = -\frac{1}{2}\mathrm{Sin}(\beta)\,\mathrm{Sin}(2\theta).
\end{aligned}
\tag{2.5}
$$

The y-oriented elements can be obtained by applying a 90-degree rotation $(4\theta \to 4\theta + \pi/2)$ to the above expressions. Finally, the total power collected by the detector is:

$$
d_{\mathrm{obs}} = \Sigma_{i=x,y}\left(\mathrm{M}^i_{TT}\ T + \mathrm{M}^i_{TQ}\ Q + \mathrm{M}^i_{TU}\ U + \mathrm{M}^i_{TV}\ V\right).
\tag{2.6}
$$

From eqs. (2.5)–(2.6), it is clear that, when $\beta = 0$, there is no contribution to the observed power from a non-vanishing V-mode signal. Conversely, the departure of the phase shift from the ideal value of π offers a handle to the detection of V modes. From eq. (2.5), we see that the V-mode signal is modulated at twice the rotational frequency (2θ). Some systematic effects caused by other HWP non-idealities (see the extended Mueller elements in the appendix of ref. [32]) also contribute to the spurious 2θ signal. As an example, imperfect reflectance and cross-polarization effects (captured by the h- and χ, ζ-parameters in eq. (2.1)) introduce 2θ-modulated leakage between Q/U and V. Disentangling V modes from purely systematic-induced signals is challenging but feasible through a combination of modeling, harmonic decomposition, and simulation-based mitigation techniques. Comprehensive modeling of the optical chain is therefore essential to separate these contributions on the basis of their distinct functional forms. Simulations are also crucial for addressing systematic contamination. By incorporating all known HWP non-idealities and their frequency-dependent effects, these simulations can generate templates of systematic signals at 2θ. These templates can then be subtracted from the observed data to isolate the V-mode signal.

The Cosmology Large Angular Scale Surveyor (CLASS) provides a valuable precedent for managing circular polarization and systematic contamination. CLASS achieved the first detection of atmospheric circular polarization at 40 GHz (see figure 2), describing it as a dipole-like pattern caused by Zeeman splitting of atmospheric oxygen. Systematic contamination was addressed by modeling the expected atmospheric signal and subtracting it from the data, as detailed in CLASS papers [34, 35].

As previously mentioned, β varies with frequency. It is possible that, at specific frequencies, β crosses 0 or 180° [36–38], such that the modulation of V modes vanishes. If a modulated signal is still observed at these frequencies, it must originate from other systematic effects. This provides a potential method for distinguishing V modes from systematics with different frequency dependencies. Identifying the frequencies where $\beta \simeq 0$ or 180°, we can compare the modulation amplitudes at these frequencies to those where $\beta \neq 0$. Genuine V-mode signals should be absent or significantly suppressed at $\beta = 0, 180°$, allowing for a clearer separation of systematic contamination.

2.2 Sensitivity to Stokes parameters

We now quantify the sensitivity to V modes of a CMB experiment equipped with a HWP with non-ideal phase shift. For the sake of simplicity, we consider Gaussian, stationary and uncorrelated instrumental noise of variance σ_{pix}^2 in real space. This simplifies the expression of the noise covariance matrix in pixel space.[3]

The square root of the diagonal elements of the inverse noise covariance in pixel space provides an estimate of the experimental noise per pixel to each Stokes parameter. In the case of a HWP with non-ideal phase shift, the noise — which we normalize to the total intensity T one — is a function of β:

$$
\begin{aligned}
\left(\frac{\sigma_{Q,U}(\beta)}{\sigma_T} \right)_{\mathrm{pix}} &= \frac{\sqrt{2}}{\mathrm{Cos}^2(\beta/2)} \\
\left(\frac{\sigma_V(\beta)}{\sigma_T} \right)_{\mathrm{pix}} &= \frac{\sqrt{2}}{\mathrm{Sin}(\beta)}.
\end{aligned}
\tag{2.7}
$$

In figure 1, we show the sensitivity to the Stokes parameters Q, U, V, normalized to the sensitivity to the Stokes T, as a function of the phase shift β. The expected noise ratio for ideal CMB experiments is $(\sigma_{Q,U}/\sigma_T)_{\mathrm{pix}} = \sqrt{2}$. The non-ideal phase shift leads to a mixing of power among the Q, U, V Stokes parameters. This can be understood from the fact that the sensitivity to Q and U decreases (i.e., the noise ratio increases, in red in figure 1) while that of V (blue) increases for larger values of β. However, while the sensitivity to V rapidly changes with β, the degradation of the sensitivity to Q, U significantly deviates from the ideal case only for fairly large values of $\beta \gtrsim 20°$ (for comparison, typical values for β vary from a few degrees up to a few tens [36–38]).

---

[3]Equation (2.6) can be generalized in matrix form as $\mathbf{d}_{\mathrm{obs}} = \mathbf{A}\,\mathbf{m} + \mathbf{n}$, where $\mathbf{d}$, $\mathbf{n}$ are vectors of the data and noise of N_t time samples, $\mathbf{m}$ is a vector of $4N_{\mathrm{pix}}$ Stokes parameters describing the sky signal in pixel space and $\mathbf{A}$ is a sparse $N_t \times 4N_{\mathrm{pix}}$ pointing matrix mapping how each pixel in the sky is converted in a time sample according to eq. (2.6). The general linear solution to the matrix equation for each pixel **pix** is given by:

$$
\hat{\mathbf{m}}_{\mathrm{pix}} = (\mathbf{A}^{\mathrm{T}}\mathbf{N}^{-1}\mathbf{A})_{\mathrm{pix}}^{-1} \, (\mathbf{A}^{\mathrm{T}}\mathbf{N}^{-1}\mathbf{d})_{\mathrm{pix}},
$$

where $\mathbf{N} = \langle \mathbf{n}\,\mathbf{n}^T \rangle$ is the noise covariance matrix in time domain and $(\mathbf{A}^{\mathrm{T}}\mathbf{N}^{-1}\mathbf{A})_{\mathrm{pix}}^{-1}$ is the noise covariance matrix in pixel space. For the simple noise properties considered in this work, i.e. $\mathbf{N} = \mathbf{diag}(\sigma^2)$, the noise covariance matrix in a pixel is simply given by $\sigma_{\mathrm{pix}}^2 = \sigma^2 \left(\mathbf{A}^{\mathrm{T}}\mathbf{A} \right)_{\mathrm{pix}}^{-1}$. This becomes $\sigma_{\mathrm{pix}}^2 = \frac{4\sigma^2}{N_{\mathrm{hit}}} \mathbf{diag}\left(1, \, 2/\cos(\beta/2)^4, \, 2/\cos(\beta/2)^4, \, 2/\sin(\beta)^2 \right)$, where N_{hit} is the number of hits on that pixel, since we assume a very homogeneous and redundant scanning strategy. See, e.g. [32] and references therein for further details.
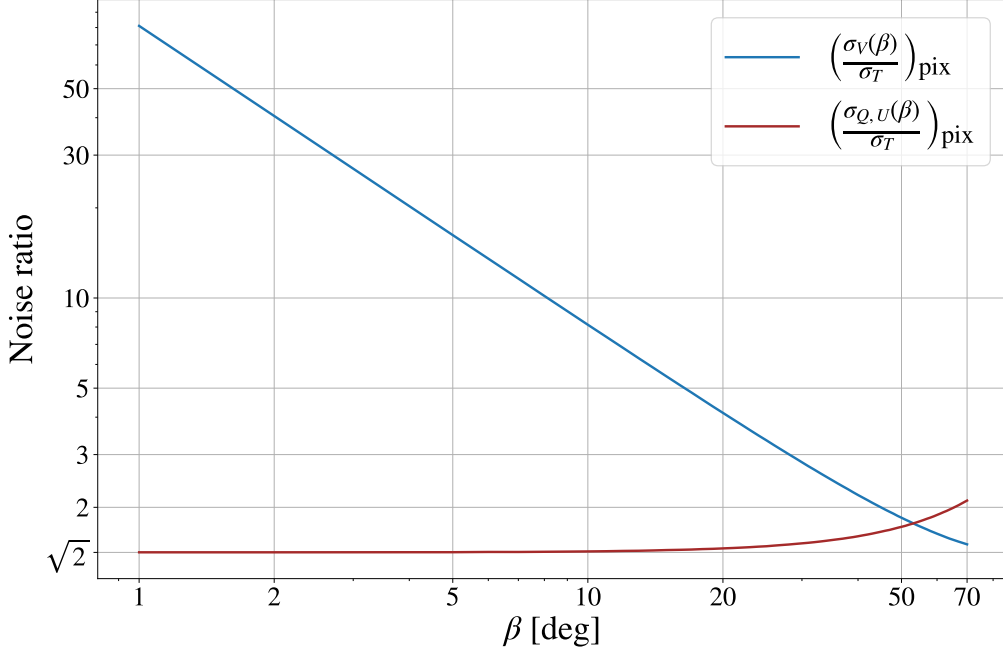
Figure 1. Noise ratio of the Stokes parameters for linear polarization $\sigma_{Q,\,U,\,\mathrm{pix}}(\beta)$ (red) and circular polarization $\sigma_{V,\,\mathrm{pix}}(\beta)$ (blue), normalized to the total intensity noise, as a function of the HWP non-ideal phase shift β. Typical values for β range from a few degrees to a few tens [36–38]. For ideal CMB experiments, $(\sigma_{Q,\,U}/\sigma_T)_{\mathrm{pix}} = \sqrt{2}$ for polarization-sensitive detectors. In presence of a non-ideal phase shift, the noise level for circular polarization $\sigma_{V,\,\mathrm{pix}}(\beta)$ decreases rapidly with increasing β, while the noise level for linear polarization $\sigma_{Q,\,U,\,\mathrm{pix}}(\beta)$ does not increase significantly until very large values of β are reached. As a result, a slightly non-ideal HWP (small value of β) can help gain sensitivity to V modes without significantly degrading the sensitivity to linear polarization.

It is also instructive to work out the sensitivity to V modes in harmonic space for a given experimental setup, as described in terms of the linear polarization noise level σ_Q, angular resolution θ_{FWHM}, observed sky fraction f_{sky} and non-ideality HWP parameter β. Note that in the rest of this section we will denote with σ_P the nominal linear polarization noise, corresponding to an ideal HWP plate, i.e. $\sigma_Q = \sigma_Q(\beta=0) = \sqrt{2}\,\sigma_T$. In this way factors of $\mathrm{Sin}\,\beta$ and $\mathrm{Cos}\,\beta$ will appear explicitly in the equations.

The observed power spectrum of the signal V modes $\hat{C}_\ell^{\mathrm{VV}}$ has an associated variance Σ_ℓ^2:

$$\Sigma_\ell^2 = \frac{2}{(2\ell+1)f_{\mathrm{sky}}} \left[C_\ell^{\mathrm{VV,fid}} + \frac{\mathrm{N}_\ell}{\mathrm{B}_\ell^2} \frac{1}{\mathrm{Sin}^2(\beta)} \right], \tag{2.8}$$

where $C_\ell^{\mathrm{VV,fid}}$ is the true underlying power spectrum of the signal, N_ℓ is the noise power spectrum of the linear polarization, assuming an ideal half-wave plate, and B_ℓ is the harmonic equivalent of a Gaussian beam of width θ_{FWHM}. We assume a white noise power spectrum $N_\ell = \sigma_Q^2$, and use a fiducial Gaussian approximation for the likelihood $\mathcal{L}(C_\ell^{\mathrm{VV}}) = \mathrm{Pr}(\hat{C}_\ell^{\mathrm{VV}}|C_\ell^{\mathrm{VV}})$ of a theoretical power spectrum C_ℓ^{VV}:

$$-2\ln\mathcal{L}(C_\ell^{\mathrm{VV}}) = \frac{(C_\ell^{\mathrm{VV}} - \hat{C}_\ell^{\mathrm{VV}})^2}{\Sigma_\ell^2}. \tag{2.9}$$

For the purpose of our analysis, we take $\hat{C}_\ell^{\mathrm{VV}} = \langle \hat{C}_\ell^{\mathrm{VV}} \rangle = C_\ell^{\mathrm{VV,fid}}$. The inverse probability $\mathrm{Pr}(C_\ell^{\mathrm{VV}}|\hat{C}_\ell^{\mathrm{VV}})$ is computed through the use of Bayes' theorem with a flat prior on C_ℓ.

Armed with the above, we compute, for each multipole ℓ, the 95% upper limit on C_ℓ^{VV} in the assumption of vanishing V-mode signal, i.e., for $C_\ell^{\mathrm{VV,fid}} = 0$, and for different experimental configurations. The results are shown in figure 2. Here, we show the results for a LiteBIRD-like satellite (black solid curve) and for a ground-based Simons Observatory/SO SAT[4] experiment (magenta dashed line), assuming $\beta = 10°$ in both cases. The other parameters describing each configuration can be read in tables 1 (noise and angular resolution) and 2 (sky coverage). For comparison, the current 95% upper bounds from the balloon-borne experiment SPIDER [27] (blue and red) and the ground-based CLASS [35, 39] (yellow and brown) along with the MIPOL polarimeter [40] are also shown. A LiteBIRD-like experiment would improve current bounds by several orders of magnitude and extend the sensitivity over a broader range of angular scales. On the other hand, a ground-based experiment like SO will dominate at smaller scales.

In figure 3, we show iso-contours of constant integrated 95% sensitivity to a scale-invariant VV spectrum, as a function of β and the instrumental noise level in linear polarization, σ_Q. In the left (right) panel, the angular resolution and sky fraction are fixed to the values corresponding the LiteBIRD (SO) experiment. The two panels also correspond to different choices of the observed multipole range, again representatives of the aforementioned experiments: $2 \leq \ell \leq 300$ in the left panel and $50 \leq \ell \leq 300$ in the right panel. As expected, the sensitivity increases for smaller values of σ_Q and large values of β. The stars in the plot indicate the expected performance of a LiteBIRD-like (left panel) and SO (right panel) experiment for $\beta = 10°$.

3 Production of V modes

In the previous section, we have quantified the sensitivity to V modes assuming a generic scale-invariant spectrum. In the following, we work out the sensitivity of different combinations of CMB experiments to a V-mode signal generated in the phenomenological framework studied in [29]. We now briefly recall the basis of this formalism.

We consider a simple class of models allowing for the in vacuo mixing of CMB polarization states during propagation, including the conversion of linear into circular polarization. The mixing of polarization states in a weakly anisotropic medium is dubbed Generalized Faraday Effect (see section 14.3 of [41] for a description of the general framework, and [28] for an application to extragalactic synchrotron sources), or GFE. As the name suggests, the usual Faraday rotation is a particular case of GFE. The radiative transfer equation for the linearly polarized radiation propagating in a weakly anisotropic non-absorbing medium reads [41]

$$\frac{\mathrm{d}}{\mathrm{d}s}\boldsymbol{S} = \boldsymbol{\rho} \times \boldsymbol{S} \tag{3.1}$$

where s is an affine parameter following the direction of wave propagation, and $\boldsymbol{S} = (Q, U, V)$

---

[4]Only the Small Aperture Telescopes (SATs) are equipped with a HWP.
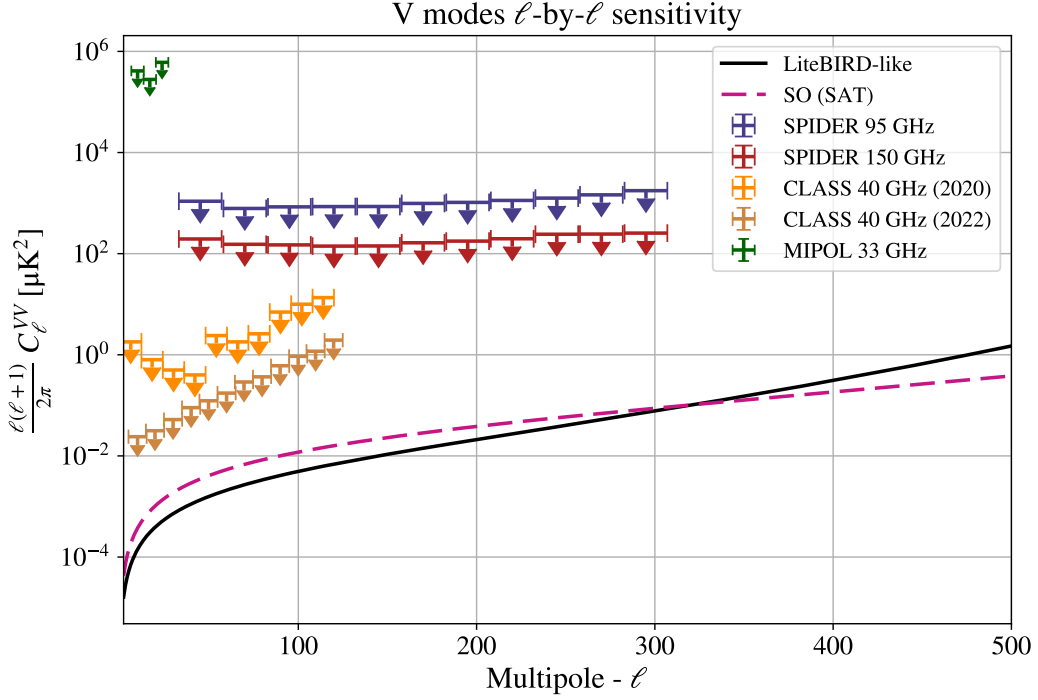
Figure 2. The figure illustrates the ℓ-by-ℓ (i.e. no binning) 95% C.L. sensitivity for current and future CMB experiments to a VV-spectrum. Assuming a non-ideal HWP with a phase shift of $\beta = 10°$, the black curve represents the sensitivity for a LiteBIRD-like experiment and the dark magenta curve corresponds to the sensitivity for a SO SAT experiment. Details on the full experimental setup adopted to obtain these curves are in table 1. For comparison, the current bounds on V modes at different frequencies and ℓ-ranges from the balloon-borne SPIDER [27] (blue and red), the ground-based CLASS [35, 39] (yellow and brown) are also shown along with the MIPOL polarimeter [40] (green).

is the polarization Stokes vector, precessing about the direction of $\boldsymbol{\rho} = (\rho_Q, \rho_U, \rho_V)$, which is determined by the dielectric tensor of the medium and thus encodes its optical properties. If $\hat{\boldsymbol{\rho}} \equiv \boldsymbol{\rho}/|\boldsymbol{\rho}|$ is directed along the V-axis in the polarization space ($\rho_Q = \rho_U = 0$), then the Stokes vector $\boldsymbol{S}$ precesses about it. The linear polarization component, i.e. the projection of S on the (Q, U) plane, will thus rotate while maintaining a constant magnitude. This is the usual Faraday rotation, where no circular polarization is generated, and only the Q and U states mix among themselves. On the other hand, if $\boldsymbol{\rho}$ has non-vanishing Q and U components, a partial conversion of linear into circular polarization occurs, generating non-zero V modes.

In ref. [29], some of us have developed a formalism that allows to derive the modifications to the CMB spectra in temperature, linear and circular polarization, and their cross-correlations, given an effective dielectric tensor that describes the optical properties of the space traversed by CMB photons. This allows to be agnostic about the specific model beyond the mixing among CMB polarization components and just capture the basic phenomenology. Therefore, once the phenomenological parameters are constrained, it is possible to interpret the results in light of a specific physical model that could have induced GFE; see, e.g. [9] for a recent application.
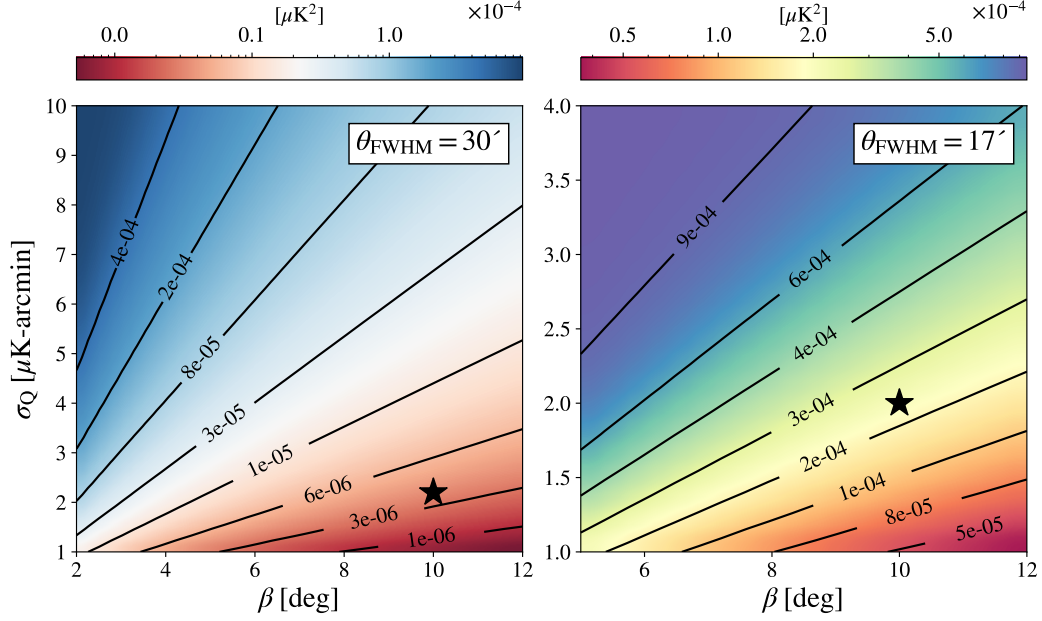
Figure 3. Contours of constant V-mode 95% sensitivity for a scale-invariant VV spectrum as function of non-ideal phase-shift β and nominal (i.e., assuming $\beta = 0$) linear polarization sensitivity $\sigma_{\rm Q}$. Left panel: the sensitivity is integrated over the multipole range $2 \leq \ell \leq 300$ for an angular resolution of 30 arcmin, similar to that achievable by LiteBIRD from space. For the LiteBIRD experiment, the expected noise level is $\sigma_Q \simeq 2.2\,\mu{\rm K}\,{\rm arcmin}$, integrated over 22 frequency channels and 3-year observation time [6]. The star marks the combination of this noise level with a value of the nonideality parameter $\beta = 10°$ (chosen arbitrarily). Right panel: the sensitivity is integrated over $50 \leq \ell \leq 300$ for an angular resolution of 17 arcmin, similar to that achievable by the ground-based SO-SAT experiment. For the SO SAT, the noise level is $\sigma_Q \simeq 2\,\mu{\rm K}\,{\rm arcmin}$, combining the 93 and 145 GHz bands [7]. The star marks the combination of this noise level with a value of the nonideality parameter $\beta = 10°$ (chosen arbitrarily).

Here we consider the case of an effective dielectric tensor that is homogeneous and independent of both the direction and magnitude of the radiation wave vector.

In this specific case, parity-violating CMB cross spectra are vanishing, TB = EB = EV = BV = 0 (see ref. [29] for details).

The remaining CMB power spectra C_ℓ^{XY} (with X, $Y = T$, E, B, V) can be expressed in terms of the CMB spectra produced at the last-scattering surface $\widetilde{C}_\ell^{XY}$:

$$
\begin{aligned}
C_\ell^{\rm TE} &= \left(1 - \frac{\beta_V^2 + \beta_E^2}{8\pi}\right) \widetilde{C}_\ell^{\rm TE} \\
C_\ell^{\rm EE} &= \left(1 - \frac{\beta_V^2 + \beta_E^2}{4\pi}\right) \widetilde{C}_\ell^{\rm EE} + \frac{\beta_V^2}{4\pi} \left[\mathcal{W}_\ell^{(1)} \widetilde{C}_\ell^{\rm EE} + \mathcal{W}_{\ell+1}^{(1)} \widetilde{C}_{\ell+1}^{\rm BB} + \mathcal{W}_{\ell-1}^{(1)} \widetilde{C}_{\ell-1}^{\rm BB}\right] \\
C_\ell^{\rm BB} &= \left(1 - \frac{\beta_V^2 + \beta_E^2}{4\pi}\right) \widetilde{C}_\ell^{\rm BB} + \frac{\beta_V^2}{4\pi} \left[\mathcal{W}_\ell^{(1)} \widetilde{C}_\ell^{\rm BB} + \mathcal{W}_{\ell+1}^{(1)} \widetilde{C}_{\ell+1}^{\rm EE} + \mathcal{W}_{\ell-1}^{(1)} \widetilde{C}_{\ell-1}^{\rm EE}\right] \\
C_\ell^{\rm VV} &= \frac{\beta_E^2}{\pi} \left[\mathcal{W}_{\ell+2}^{(2)} \widetilde{C}_{\ell+2}^{\rm BB} + \mathcal{W}_{\ell+1}^{(2)} \widetilde{C}_{\ell+1}^{\rm EE} + \mathcal{W}_\ell^{(2)} \widetilde{C}_\ell^{\rm BB} + \mathcal{W}_{\ell-1}^{(2)} \widetilde{C}_{\ell-1}^{\rm EE} + \mathcal{W}_{\ell-2}^{(2)} \widetilde{C}_{\ell-2}^{\rm BB}\right],
\end{aligned}
\tag{3.2}
$$
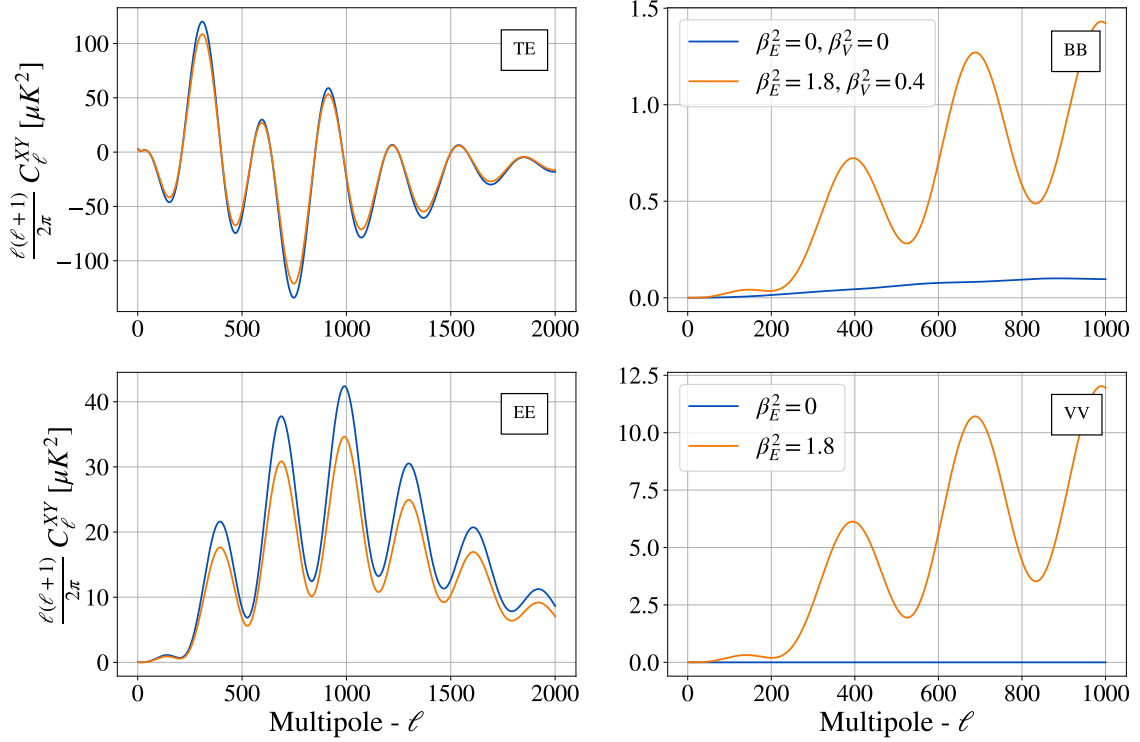
Figure 4. Impact of Generalized Faraday Effect (GFE) on polarization power spectra. The reference (blue) power spectra are computed using Planck best-fit values from TT, TE, EE, lowE + lensing [1] and vanishing GFE parameters, as reported in table 3, while the modified spectra (orange) are calculated fixing $\beta_V^2 = 0.4$ and $\beta_E^2 = 1.8$ (chosen arbitrarily to make the GFE visible).

where $\mathcal{W}^{(1,2)}$ are combinations of Wigner $3j$-symbols, and the phenomenological parameters β_E^2 and β_V^2 are, respectively, combinations of the diagonal and off-diagonal components of the effective susceptibility tensor [29].

From eqs. (3.2) and figure 4, it is clear that the modification of the CMB polarization signal due to this particular realization of GFE has three main effects:

- rescaling of the amplitude of TE, EE, BB spectra via the combination $\beta_V^2 + \beta_E^2$;

- mixing between E and B modes (cosmic birefringence), proportional to β_V^2;

- sourcing of V modes from E and B modes, proportional to β_E^2.

4   Analisys method and datasets

In this section, we present methodology and data employed in the likelihood analysis. We simulate the performance of different upcoming CMB experiments (satellite and ground-based) and forecast their sensitivity to the phenomenological GFE parameters $\beta_{E,V}^2$ introduced in the previous section. To this scope, we perform a Monte Carlo Markov Chain (MCMC) analysis to obtain forecasted constraints on β_E^2 and β_V^2 jointly with the six ΛCDM parameters

and the tensor-to-scalar ratio r.[5] We use a customized version[6] of the `CosmoMC` [42] package to perform the analysis. We assume convergence of the MCMC chain by requiring that the Gelman-Rubin statistics $R - 1 \sim 0.01$.

We run forecasts for five combinations of data sets which simulate the performance of different CMB experiments:

- a future LiteBIRD-like satellite experiment. We refer to this case as "L";

- LiteBIRD-like in combination with a simulated version of the Planck data, labeled "LP";

- a currently running Simons Observatory (SO) ground-based experiment, in combination with Planck, labeled "PSO". We include simulated performance of the observations with both the Large Aperture Telescope (LAT) which targets the smallest angular scales and the array of Small Aperture Telescopes (SATs) which target B modes at degree angular scales. The HWP is deployed on SATs only;

- Planck in combination with a next-generation ground-based experiment, i.e. CMB-S4-like, labeled "$PS4$". As for SO, we include information from both LAT and SATs. We note that the baseline design of CMB-S4, as described in [8, 43], does not include a HWP. Therefore, when referring to a CMB-S4-like experiment, we actually refer to the combination of expected sensitivity as determined by the sky coverage, angular resolution and noise properties reported in [8, 43], augmented with the use of a HWP in the telescopes targeting B modes to modulate the polarization signal;

- LiteBIRD-like in combination with CMB-S4-like, labeled "$LS4$".

The instrument characteristics of each simulated experiment are reported in table 1. In the following, when referring to individual experiments, we will omit the "like" suffix for brevity.

As anticipated, for the sake of simplicity, we do not make use of the real data collected by Planck. We instead consider a simple white noise spectrum with 40 μK-arcmin in temperature, and 80 μK-arcmin in polarization [46], which reasonably reproduces the Planck performance. The noise spectrum for LiteBIRD is computed given the detector sensitivity and the angular resolution of LiteBIRD in the central frequency channels [6]. For SO [7], we make use of the publicly available noise curves.[7] The latter also include residual contributions from component separation, which dominates the cosmological signal both at the very small scales probed by the SO LAT, as well as at the intermediate scales probed by the SO SAT. CMB-S4 noise curves were computed referring to the central channels for both SAT and LAT [8].

---

[5]The full set of sampled parameters is as follows: the angular scale of the sound horizon at recombination, θ, the cold dark matter and baryon physical densities today, $\omega_{\rm cdm}$ and ω_b respectively, the amplitude and spectral index of the spectrum of primordial scalar perturbations, $\log(10^{10}A_s)$ and n_s respectively, the optical depth to reionization τ, the tensor-to-scalar ratio r and the GFE phenomenological parameters β_E^2 and β_V^2. We assume adiabatic initial conditions and consider inflation consistency, which allows to express the spectral index of tensor perturbations as $n_t = -r/8$. We consider one massive neutrino of mass $m_\nu = 0.06\,{\rm eV}$ and two massless neutrinos, for a total number of relativistic degrees of freedom at recombination of $N_{\rm eff} = 3.044$.

[6]The code is publicly available at this link: https://github.com/nraffuzz/CosmoMC_GFE.

[7]SO noise curves are available at https://github.com/simonsobs/so_noise_models.

Experiment	Noise [μK-arcmin]	Beam size [arcmin]	Phase-shift β [°]
LiteBIRD	2	30	0/10
Planck	40	7	—
SO LAT	6.5	1.4	—
SO SAT	2	17	0/10
S4-like LAT	3	1.5	—
S4-like SAT	1	30	0/10

Table 1. Instrumental specifications for each experiment: sensitivity to total intensity in μK-arcmin (linear polarization sensitivity is obtained by multiplying this value by a $\sqrt{2}$ factor, except for Planck which is 2 as only half the detectors are polarized); beam size FWHM in arcmin; non-ideal phase shift in degrees (for those experiments that will deploy — or we simulate will deploy — a HWP [7, 43, 44]). The noise levels for SO SAT and LAT are reported for reference. They are coadded over the central 90 and 150 GHz channels, and the FWHM corresponds to the 145 GHz channel. For more details, see [7, 45]. In this work, we make use of the official SO noise curves.

When adding V-mode data in the analysis, the noise spectra of LiteBIRD, SO and CMB-S4 are further rescaled to account for the non-ideal phase shift, as detailed in section 2. In practice, the rescaled noise curves become:

$$
\begin{aligned}
\frac{N_\ell^{EE}}{B_\ell^2} &\to \frac{1}{B_\ell^2}\frac{N_\ell^{EE}}{\text{Cos}^4(\beta/2)} \\
\frac{N_\ell^{BB}}{B_\ell^2} &\to \frac{1}{B_\ell^2}\frac{N_\ell^{BB}}{\text{Cos}^4(\beta/2)} \\
\frac{N_\ell^{VV}}{B_\ell^2} &\to \frac{1}{B_\ell^2}\frac{N_\ell^{VV}}{\text{Sin}^2(\beta)}.
\end{aligned}
\tag{4.1}
$$

Note that Planck/CMB-S4 and LiteBIRD experiments observe largely overlapping sky fractions. While LiteBIRD dominates over Planck in B-mode sensitivity, the performance of the two experiments are different in T and E modes at different angular scales, depending on the respective noise level and angular resolution. A similar consideration applies to the combination "*LS4*" as far as the T and E-fields ("TE" hereafter) are concerned. Therefore, for the "TE" fields in the "*LP*" and "*LS4*" cases, we use an effective inverse noise weighted curve:

$$
N_\ell^{\text{eff}} = \left[\left(\frac{N_\ell}{B_\ell^2}\right)_X^{-1} + \left(\frac{N_\ell}{B_\ell^2}\right)_{\text{LiteBIRD}}^{-1} \right]^{-1},
\tag{4.2}
$$

where $X =$ Planck, CMB-S4. We can distinguish two regions where the two experiments perform differently: LiteBIRD dominates at larger scales, whereas Planck or CMB-S4 outperform LiteBIRD at smaller angular scales.

Differently, when Planck is combined with SO/CMB-S4, information from the former is only included in the sky fraction and/or at the angular scales not observed by SO/CMB-S4(LAT). As a result, in the "*PSO/PS4*" case, we make use of the individual noise curves for each experiment.

We employ an exact likelihood in harmonic space, rescaled by a ℓ-independent sky fraction $f_{\rm sky}$ to account for the experiment-specific sky coverage.

$$-2\ln\mathcal{L}_\ell = f_{\rm sky}(2\ell+1)\left(\mathrm{Tr}\left[\hat{\mathbf{S}}_\ell\mathbf{S}_\ell^{-1}\right]+\ln\det[\mathbf{S}_\ell]\right)+\ \mathrm{const.} \qquad (4.3)$$

where $\hat{\mathbf{S}}$ and $\mathbf{S}$ are matrices of the "observed" (i.e., simulated, in our case) $\hat{C}_\ell$ and theoretical C_ℓ power spectra, respectively (see, e.g., section 2.2 of [47] for the definition of $\hat{\mathbf{S}}$ and $\mathbf{S}$). When V modes are included in the likelihood analysis, the standard $\hat{\mathbf{S}}$ and $\mathbf{S}$ matrices are extended to include the $C_\ell^{\rm VV}$. The sky fraction, range of angular scales and observed fields for each data combination[8] are reported in table 2.

We simulate the observed spectra $\hat{C}_\ell$ as the sum of a reference set of CMB spectra obtained with the Boltzmann code camb [48] from a fiducial set of cosmological parameters and the noise power spectrum in harmonic space: $\hat{C}_\ell = C_\ell^{\rm fid} + \mathrm{N}_\ell/\mathrm{B}_\ell^2$ (see, e.g., section 3.3 of [47] for the extension of the definition of $\hat{\mathbf{S}}$ and $\mathbf{S}$ in eq. (4.3) in presence of noise and beam smearing). We assume the fiducial model to be ΛCDM, i.e., vanishing V-mode signal and vanishing primordial tensor modes. The cosmological parameters corresponding to the fiducial model are reported in table 3. A major source of variance in the observation of primordial B modes is the BB lensing contribution, which can be significantly reduced via appropriate de-lensing procedures. In order to quantify the effect of delensing in our results, we consider two cases: a fully lensed fiducial BB, i.e., no de-lensing, and a partly de-lensed fiducial BB. The two cases are obtained by properly rescaling the BB lensing contribution (in both the fiducial and the theory BB spectra) by a factor $A_{\rm L} = 1$ (fully lensed) and $A_{\rm L} = 0.3$ (70% de-lensing). The GFE-modified (tensorial) B modes are later summed to the $A_{\rm L}$-rescaled lensed B modes. The underlying assumption, also used in ref. [29], posits that GFE exclusively affects primordial B modes, even though GFE and lensing should occur simultaneously as integrated effects along the line of sight. This assumption is valid for LiteBIRD and SO, see, e.g., [29]. However, for fourth-generation ground-based experiments such as CMB-S4, caution is advised regarding the interplay between lensing and GFE. In order to assess the validity of the assumption for CMB-S4, we compute the difference between the BB spectrum obtained as detailed above and the BB spectrum obtained by applying GFE to the sum of tensor and lensing BB spectra. We then compare this difference with the CMB-S4 noise curve. We find that, for reasonably small values of GFE parameters ($\beta_{E,V}^2 \lesssim 0.1$), the difference in the predicted CMB spectra between the two approaches is well below the noise contribution. Furthermore, other studies in the literature, such as ref. [49], have confirmed that lensed B modes have a negligible impact on cosmic birefringence.

To better quantify the impact of a potential sensitivity to V modes, we compare results obtained with and without the inclusion of V modes in the datasets for each combination of experiments. We refer to the two cases as "TEBV" and "TEB", respectively. In the "TEBV" case, we assume the non-ideal phase shift to be $\beta = 10°$; as already noted, this choice is

---

[8]A note on the "*PSO*" dataset observing TTTEEE (SO-LAT plus Planck): SO-LAT can at most cover 40% of the sky, therefore we set Planck to observe the remaining 30% of the sky to match an overall sky coverage of 70% as in other cases. Similarly, for the "*LS4*" dataset on the combination observing TTTEEE (S4-LAT and LiteBIRD plus LiteBIRD alone): S4-LAT can at most cover 60% of the sky, therefore we set LiteBIRD alone to observe the remaining 10% of the sky to match the 70% sky coverage.

Label	Experiment	Multipoles	Fields	$f_{\rm sky}$
L	LiteBIRD	2,1000	TEB/TEBV	0.7
LP	LiteBIRD & Planck	2,1500	TE	0.7
	Planck	1501,2500	T	0.7
	LiteBIRD	2,1000	B/BV	0.7
PSO	Planck	2,50	TE	0.7
	Planck	51,2500	TE	0.3
	SO LAT	51,3000	TE	0.4
	SO SAT	50,300	B/BV	0.1
PS4	Planck	2,50	TE	0.7
	Planck	51,2500	TE	0.1
	S4-like LAT	51,3000	TE	0.6
	S4-like SAT	50,300	B/BV	0.03
LS4	LiteBIRD	2,50	TEB/TEBV	0.7
	LiteBIRD	51,1000	B/BV	0.7
	S4-like LAT & LiteBIRD	51,3000	TE	0.6
	LiteBIRD	51,1000	TE	0.1
	S4-like SAT	50,300	B/BV	0.03

Table 2. Data combinations considered in this work. For each experiment, we report the observed fields (temperature T, linear polarization E and B, circular polarization V) and the corresponding range of angular scales (multipoles), as well as the sky fraction observed ($f_{\rm sky}$). Throughout the main text, we refer to each combination with the corresponding label in the first column.

Cosmological parameter	Fiducial value
$\Omega_{\rm b}h^2$	0.02237
$\Omega_{\rm c}h^2$	0.1200
$100\theta_{\rm MC}$	1.04092
τ	0.0544
$\ln(10^{10}{\rm A_s})$	3.044
$n_{\rm s}$	0.9649
r	0
β_E^2	0
β_V^2	0

Table 3. Fiducial values of cosmological parameters for the reference cosmological model assumed to simulate the observed CMB spectra in this analysis. They are taken from the Planck best-fit values from TT, TE, EE + lowE + lensing analysis [1].

in agreement with the expected values of the phase shift from simulations. In addition, as shown in figure 1, this value allows concurrently for a relatively acceptable noise level in V-Stokes parameter and negligible degradation of the noise level in Q/U-Stokes. In the "TEB" case, we assume the phase shift to be $\beta = 0$.

5 Results

In this section, we present and discuss the results obtained for the various datasets and cases introduced in the previous section. These results are also compared with the current bounds reported in literature [29, 50]. We focus on a subset of cosmological parameters: the optical depth (τ), the tensor-to-scalar ratio (r), and the GFE parameters (β_E^2 and β_V^2).[9] The first two parameters are linked to the primary science goals of experiments observing large and intermediate-scale polarization, such as LiteBIRD, SO, and CMB-S4, while the latter two are the main focus of this study. The 68% C.L. constraints on τ and the 95% C.L. upper bounds on the remaining three parameters are in table 4 for both the fully lensed and partially de-lensed scenarios. Marginalized 1D and 2D posterior probabilities for r, τ, β_E^2 and β_V^2 can be found in the figures in appendix A. We compare the results obtained with and without the inclusion of V-mode data. In doing so, we expect to place more stringent limits on β_E^2 and β_V^2. In addition, we test whether the partial degradation of sensitivity to linear polarization resulting from a non-ideal phase shift affects the constraints on τ and r.

From table 4, we can draw the following considerations:

- as known, the constraints on τ and r are driven by the ability of a given data combination to recover the large-scale E-mode signal and the large-to-intermediate B-mode signal respectively. In table 4, compare, e.g., the improvement of the constraints on τ from the combinations including LiteBIRD with respect to those including Planck. Similarly, compare the lack of improvement of the constraints on r from the "L" dataset with respect to the "LP" combination.

  Ignoring for a moment the impact of V-mode observations (but see the second bullet point below), the constraints on β_E^2 are mostly driven by the ability to reconstruct the TE and EE spectra at intermediate and small scales, since β_E^2 acts as an overall rescaling factor for the CMB spectra (see eqs. (3.2)). Indeed, by comparing the first rows of each Dataset box in table 4, we note a steady improvement of the constraints on β_E^2 when considering dataset which are more and more sensitive to small-scale E (compare, e.g., "L" and "LP"; also, note the lack of improvement when comparing "$PS4$" with "$LS4$", as CMB-S4 dominates the sensitivity to E in both data combinations).

  The constraints on β_V^2 are mostly driven by the sensitivity of each dataset to B modes, both via the overall rescaling of the amplitude (first term on the r.h.s. in eq. (3.2)) and via the mixing with E modes (second term on the r.h.s.).[10]

- the addition of V-mode data tightens the constraints on β_E^2 by roughly an order of magnitude but has no effect on β_V^2 (compare the two rows corresponding to each data

---

[9]We do not report constraints on other parameters beyond these, as the impact of β_E^2 and β_V^2 on the rest of the parameter space is beyond the scope of this paper and, in any case, any effect is negligible. See, e.g., [9] for further details.

[10]The same mixing term appears on the r.h.s. of the equation for C_ℓ^{EE}. However, this term is negligible with respect to the first one appearing on the r.h.s. of the same equation, since the amplitude of $\tilde{C}_\ell^{\mathrm{BB}}$ (as well as the amplitude of the $\tilde{C}_\ell^{\mathrm{EE}}$ weighted by the Wigner coefficients) is significantly lower than the amplitude of $\tilde{C}_\ell^{\mathrm{EE}}$. Therefore, E-mode observations do not play a significant role in constraining β_V^2 compared to B-mode observations.

label in table 4; see also appendix A). Indeed, $C_\ell^{\rm VV}$ in eq. (3.2) is solely affected by β_E^2 that acts as an overall rescaling factor of a mixing of $\tilde{C}_\ell^{\rm EE}$ and $\tilde{C}_\ell^{\rm BB}$. The inclusion of V modes, with the corresponding rescaling of the noise spectra as per eq. (4.1) and figure 1, does not degrade the constraints on r and τ. This is one of the main findings of this work. This stands in contrast to the assertion made in [29] regarding the necessity of improving linear polarization for increased accuracy on GFE parameters. The inclusion of V-mode data proves to be an additional, significant source of constraining power, beyond what is provided by linear polarization alone. The sensitivity (i.e. the low VV noise) is enhanced by the non-ideal phase shift of the HWP (as shown in figure 1), where a relatively conservative value of $\beta = 10°$ was employed;

- by reducing the contribution of signal variance in the observation of primordial B modes, the de-lensing procedure results in a factor of two improvement of the constraints on r and β_V^2 (compare rows with the same data label in the top and bottom panels in table 4). No improvement is seen for τ and β_E^2, as could be visually verified by comparing the left (no de-lensing) with the right (70% de-lensing) panel of triangular plots in appendix A. This confirms that the constraining power on these parameters comes essentially from TE and EE spectra rather than from BB (in addition to VV for β_E^2).

  Improvements on r and β_V^2 are expected, since they directly impact the $C_\ell^{\rm BB}$ power spectrum as rescaling factors. In eq. (3.2), we recognize an attenuating factor $(\beta_V^2 + \beta_E^2)/4\pi$ in front of the unmodified $\tilde{C}_\ell^{\rm BB}$. In the second term on the r.h.s., the amplitude of the combination of unmodified EE and BB spectra — with the $\tilde{C}_\ell^{\rm BB}$ spectrum being subdominant compared to the unmodified $\tilde{C}_\ell^{\rm EE}$ — is regulated by β_V^2. This requires β_V^2 to suppress the power coming from the EE spectrum, thus restoring the expected amplitude of the observed tensorial B modes ($r = 0$).

  Also, de-lensing does not help improve the constraining power on the optical depth τ. In principle, information on τ can be also extracted from measurements of the reionization peak in the BB spectrum. However, the strong degeneracy between r and τ in that region as well as the residual lensing variance dominating also at low-ℓs for vanishingly small values of r severely limit the information content that can be extracted from BB to improve the constraints on τ. As a result, the constraining power for this parameter comes essentially from E modes only;

- when comparing the constraints on r from "*PSO*" and "*PS4*" in the fully lensed case (top panel in table 4), we note that the latter dataset provides — somehow unexpectedly — a looser bound on r than the former dataset (see also left panels of figures 7 and 8). This feature can be attributed to the fact that the two experiments driving the constraints on r in the two data combinations — namely, SO and CMB-S4 — are both cosmic variance limited in BB in the fully lensed scenario. With the instrumental noise being subdominant, the ability to jointly constrain the parameters affecting $C_\ell^{\rm BB}$ is solely determined by volume effects in the parameter space explored in the MCMC analysis. More in detail, at first order, we can assume that the amplitude of $C_\ell^{\rm BB}$ is determined by a combination of r, β_E^2 and β_V^2 (see eqs. (3.2)). When switching from "*PSO*" to "*PS4*" data combination, the enhanced sensitivity of the latter to E modes leads to

more stringent limits on β_E^2, thus allowing for a larger excursion of r in parameter space. For the same reason, the constraints on β_V^2 from the two data combinations are virtually unchanged. In this case, the volume effect responsible for the degradation of the constraints on r is suppressed for β_V^2 by the extra contribution of the E-B mixing term on the r.h.s. in the equation for C_ℓ^{BB}.

Conversely, for partial de-lensing (bottom panel of table 4; see also right panels of figures 7 and 8), we observe the expected improvement of the constraint on r when moving from "*PSO*" to "*PS4*". While "*PS4*" remains cosmic variance limited, the impact of instrumental noise in "*PSO*" cannot be neglected and washes out the volume effect described above.

Finally, in table 5 we quote again the 95% C.L. upper limits for the five analyzed cases combining TEBV modes, and compare them with current bounds. We note that current limits in the literature are obtained without a de-lensing procedure applied to data. Nevertheless, we report forecasts for both the fully lensed and the partially de-lensed scenarios, to also assess the benefit of de-lensing. The current upper limit on r is taken from the analysis of BICEP2, Keck Array, BICEP3, WMAP, and Planck data, marginalizing over a given model of Galactic dust and synchrotron contaminations [50]. As already mentioned, no de-lensing is applied to the data. Future experiments targeting r will see considerable improvement in the constraints by applying suitable de-lensing techniques (see, e.g., [8, 51, 52]). Our forecasts qualitatively confirm this expectation. Present bounds on $\beta_{E,V}^2$ are taken from the analysis of [29] and were derived using temperature and linear polarization anisotropies from the Planck legacy release [53] and BICEP2/Keck 2015 [54]. The inclusion of current V-mode observations does not help improve the constraints on the GFE parameters [29]. Forecasted sensitivity to β_V^2 is dominated by the sensitivity of upcoming experiments to B modes, with de-lensing playing a crucial role. As far as β_E^2 is concerned, while de-lensing has minimal impact on the forecasted sensitivity, the inclusion of V modes from future experiments significantly improves the constraints. Our forecast shows that more stringent constraints ranging from 1 to 3 orders of magnitude can be achieved, depending on the considered parameter and dataset.

6   Conclusions

In this study, we investigated how the deployment of a realistic half-wave plate (HWP) inducing a non-ideal (i.e., $\neq \pi$) phase shift, may affect the noise characteristics of CMB experiments, while providing sensitivity to the presence of a non-vanishing V-mode signal. We then forecasted the expected performance of new-generation CMB experiments, noting that our analysis did not consider foregrounds.

Deviations from the ideal phase shift modify the noise properties of a CMB experiment deploying a HWP by degrading the sensitivity to Q/U polarization. This could potentially spoil the ability to reach the primary science goals of future CMB experiments, such as a CVL determination of the optical depth τ and a tight constraint on/high-significance detection of the tensor-to-scalar ratio r. However, at the same time, deviations from the ideal performance of a HWP allow for the experiment to become sensitive to possibly non-vanishing V modes in the observed signal. This work showed how even a significant deviation from the ideal phase

Dataset ($A_{\rm L} = 1$)	Fields	τ	$\beta_E^2\ [10^{-2}]$	$\beta_V^2\ [10^{-3}]$	$r\ [10^{-3}]$
L	TEB	$0.0543^{+0.0019}_{-0.0021}$	< 9.7	< 1.1	< 0.4
	TEBV	0.0544 ± 0.0020	< 0.5	< 1.1	< 0.4
LP	TEB	$0.0544^{+0.0019}_{-0.0021}$	< 8.4	< 1.1	< 0.4
	TEBV	$0.0544^{+0.0018}_{-0.0021}$	< 0.5	< 1.1	< 0.4
PSO	TEB	0.0547 ± 0.0040	< 6.6	< 4.2	< 4.4
	TEBV	0.0546 ± 0.0040	< 2.9	< 4.3	< 4.4
PS4	TEB	$0.0548^{+0.0034}_{-0.0038}$	< 5.1	< 4.5	< 5.7
	TEBV	$0.0547^{+0.0034}_{-0.0038}$	< 1.0	< 4.4	< 5.0
LS4	TEB	$0.0544^{+0.0017}_{-0.0020}$	< 5.1	< 0.9	< 0.4
	TEBV	0.0544 ± 0.0019	< 0.5	< 0.8	< 0.4

Dataset ($A_{\rm L} = 0.3$)	Fields	τ	$\beta_E^2\ [10^{-2}]$	$\beta_V^2\ [10^{-3}]$	$r\ [10^{-3}]$
L	TEB	$0.0543^{+0.0018}_{-0.0021}$	< 9.8	< 0.6	< 0.2
	TEBV	$0.0544^{+0.0018}_{-0.0021}$	< 0.5	< 0.6	< 0.2
LP	TEB	$0.0543^{+0.0018}_{-0.0021}$	< 8.7	< 0.6	< 0.2
	TEBV	0.0544 ± 0.0019	< 0.5	< 0.6	< 0.2
PSO	TEB	$0.0549^{+0.0037}_{-0.0041}$	< 6.6	< 2.5	< 2.5
	TEBV	$0.0549^{+0.0038}_{-0.0043}$	< 3.0	< 2.6	< 2.5
PS4	TEB	0.0549 ± 0.0036	< 5.2	< 1.8	< 2.0
	TEBV	0.0547 ± 0.0037	< 1.0	< 1.8	< 2.0
LS4	TEB	0.0545 ± 0.0019	< 5.3	< 0.5	< 0.2
	TEBV	$0.0545^{+0.0017}_{-0.0020}$	< 0.5	< 0.5	< 0.2

Table 4. Constraints on a subset of cosmological parameters sampled in this analysis: 68% C.L. constraints for the optical depth (τ), and 95% C.L. upper limits for the tensor-to-scalar ratio (r) and the GFE parameters (β_E^2, β_V^2). The results are shown assuming a lensing factor $A_{\rm L} = 1$ (no de-lensing, top table) and $A_{\rm L} = 0.3$ (70% de-lensing efficiency, bottom table), for different data combinations (*L*, *LP*, *PSO*, *PS4*, and *LS4*). For each data combination, we compare the results obtained with and without the inclusion of V-mode observations.

Dataset	95% C.L. ($A_{\rm L} = 1$)			95% C.L. ($A_{\rm L} = 0.3$)		
	β_E^2 [10^{-2}]	β_V^2 [10^{-3}]	r [10^{-3}]	β_E^2 [10^{-2}]	β_V^2 [10^{-3}]	r [10^{-3}]
L	< 0.5	< 1.1	< 0.4	< 0.5	< 0.6	< 0.2
LP	< 0.5	< 1.1	< 0.4	< 0.5	< 0.6	< 0.2
PSO	< 2.9	< 4.3	< 4.4	< 3.0	< 2.6	< 2.5
$PS4$	< 1.0	< 4.4	< 5.0	< 1.0	< 1.8	< 2.0
$LS4$	< 0.5	< 0.8	< 0.4	< 0.5	< 0.5	< 0.2
Current bounds	< 14	< 30	< 36			

Table 5. 95% C.L upper limits on the tensor-to-scalar ratio and GFE parameters (β_E^2 and β_V^2) for the different data combinations considered in this analysis. These limits are obtained from the analysis of T, E, B and V modes, with a lensing factor $A_{\rm L} = 1$ (second, third and fourth columns) and $A_{\rm L} = 0.3$ (last three columns). In the last row, bounds on the same parameters from current data [29, 50] are also reported to ease the comparison, where no de-lensing procedures are included.

shift (of the order of $10°$) can open a window to the investigation of beyond-the-standard-model (BSM) cosmological scenarios while having no impact on the sensitivity to τ and r.

As a test case, we focused on the phenomenology of a class of models leading to BSM electromagnetic effects on the CMB, the Generalized Faraday Effect (GFE) [29]. The GFE is responsible for E-B mixing as well as for sourcing circular polarization from the conversion of linear CMB polarization. These effects are modeled via two phenomenological parameters — β_E^2 and β_V^2 — which modify the shape of the CMB spectra as they emerge from the last scattering surface (eqs. (3.2)). We forecasted the sensitivity to these parameters from currently running and future CMB experiments which will or might deploy a HWP. At the same time, we checked that the sensitivity to τ and r expected from these experiments is not degraded. We considered different combinations of simulated data from a LiteBIRD-like satellite experiment (L), from the ground-based Simons Observatory (SO) and a modified version (i.e., with the inclusion of a HWP) of a ground-based CMB-S4-like experiment ($S4$).[11] We also included information from Planck (P) observations where relevant.

By comparing the results with current limits in the literature [29], we forecasted a 1-to-3 order-of-magnitude improvement of the constraints on β_V^2 and β_E^2, depending on the dataset, with the most stringent limits achieved with the "$LS4$" combination (see table 5).

The possibility to include observations of V modes, as enabled by the deployment of a realistic HWP, is key to obtain dramatic improvements in the constraints on β_E^2, ranging from a factor of a few for the combinations "PSO" and "$PS4$" to an order of magnitude and more for the data combinations including LiteBIRD (see table 4). Better sensitivity to intermediate-to-small scale E modes is also an important driver of the improved constraints on β_E^2, as can be noted by comparing "L", "LP", "PSO"/"$PS4$". Constraints on β_V^2 are mostly insensitive to the inclusion of V modes in the analysis. Instead, they are driven by improved sensitivity to B modes. The constraints improve roughly by a factor of two

---

[11]We remind the reader that the baseline configuration of CMB-S4 does not include the HWP. In this work, we considered the possibility to deploy a HWP as a way to test the performance of a future ground-based experiment with the expected sensitivity and angular resolution of CMB-S4.

when partial de-lensing (obtained as a 70% suppression of lensing power in the simulated BB data) is applied in the analysis (compare the top and bottom panels in table 4). The stringent constraints on β_V^2 and β_E^2 will provide valuable insights on the fundamental physics governing the evolution of the Universe, particularly from the CMB last scattering to the present epoch. The GFE parameters can be mapped onto the elements of an effective "cosmic susceptibility tensor", which describes the optical properties of the Universe seen as the medium through which CMB photons propagate. The mapping between β_V^2 and β_E^2 and the elements of the susceptibility tensor can be obtained once a specific physical model responsible for the GFE is specified. As such, constraints on β_V^2 and β_E^2 shed light on the nature of the GFE and its potential origins, such as magnetic fields [22, 23, 41, 55–57] or other BSM phenomena [9, 16, 17, 21, 58] that could have influenced the polarization state of the CMB. The methodology outlined in this work can be also applied to models capable of generating parity-breaking spectra (e.g. ref. [9]). In conclusion, the results presented in this study indicate that the possibility of including observations of V modes in the cosmological analysis is a key tool to investigate more deeply specific aspects of fundamental physics which are otherwise less accessible, without spoiling the constraining power to other primary science targets. This emphasizes the necessity of fully exploit the potential of upcoming CMB experiments, including the extraction of V-mode data, which will provide unprecedented insights on the fundamental physics of the early Universe.

Acknowledgments

## A   Complete set of triangular plots

We show here the triangular plots for the five cases analyzed, displaying 1D and 2D posteriors for the parameters we consider relevant in our analysis, i.e. r, τ, β_E^2 and β_V^2. The general behaviour of all plots looks similar, the inclusion of V-mode polarization substantially enhances our constraining power improving the bound on β_E^2. Furthermore, the addition of the de-lensing procedure is effective in reducing the upper limits of r and β_V^2 (see the right panel of figures 5, 6, 7, 8, 9). In contrast, as expected, bounds on τ were found to be unaffected by both the de-lensing and the addition of V-mode data.
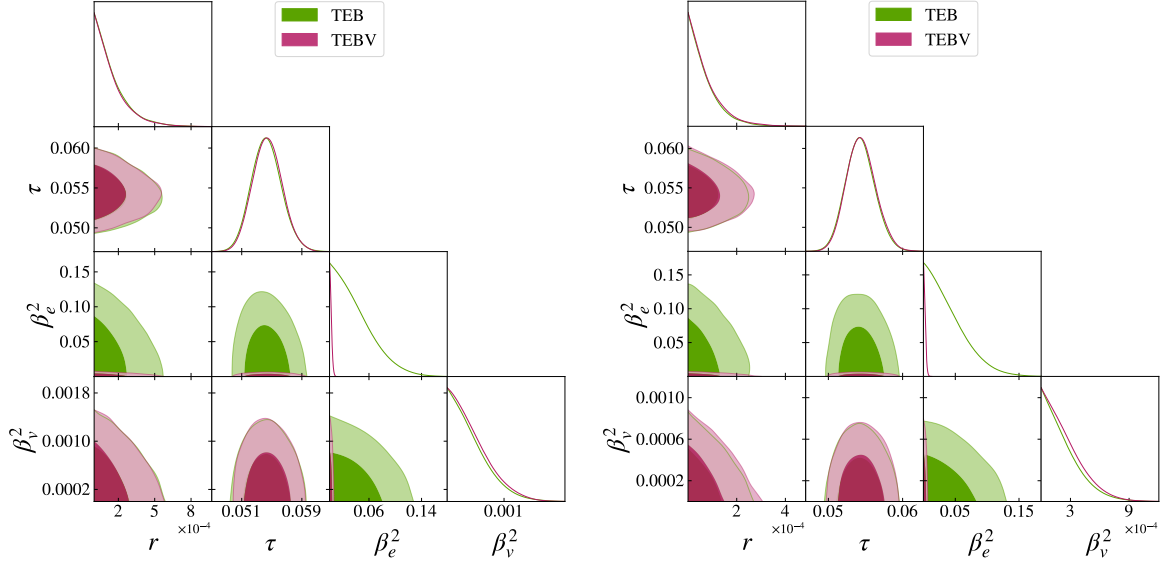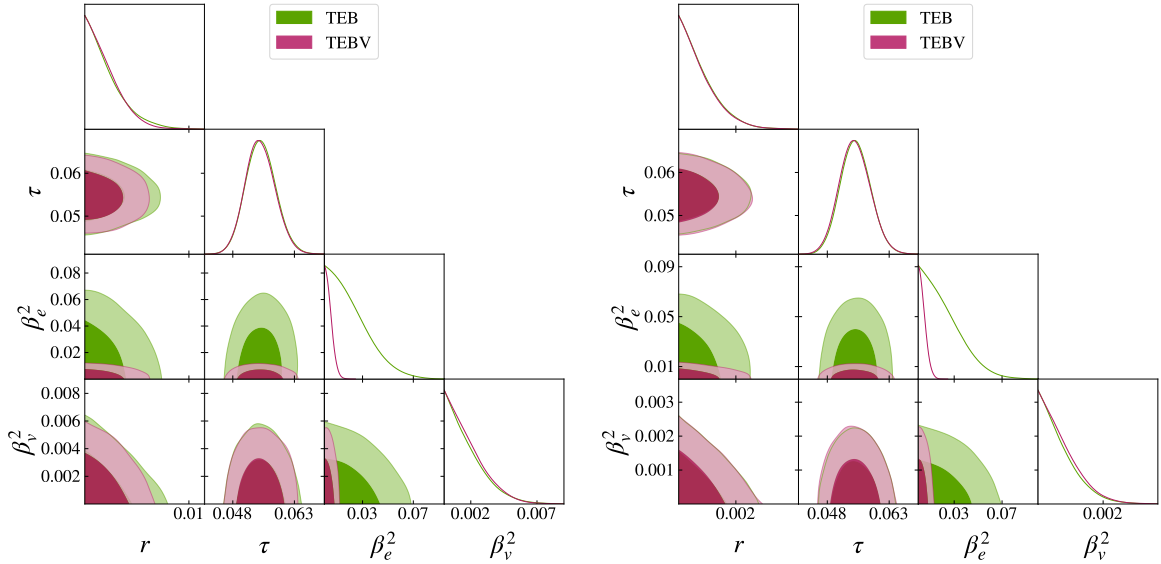
Figure 5. One and two-dimensional posterior probability distributions for L dataset (see table 2 for details). We report a subset of the total parameter space (ΛCDM model $+ r + \beta_E^2 + \beta_V^2$) showing TTTEEEBB in green and TTTEEEBBVV in magenta. The left panel omits de-lensing procedures ($A_L = 1$), while the right panel employs 70% de-lensing ($A_L = 0.3$).
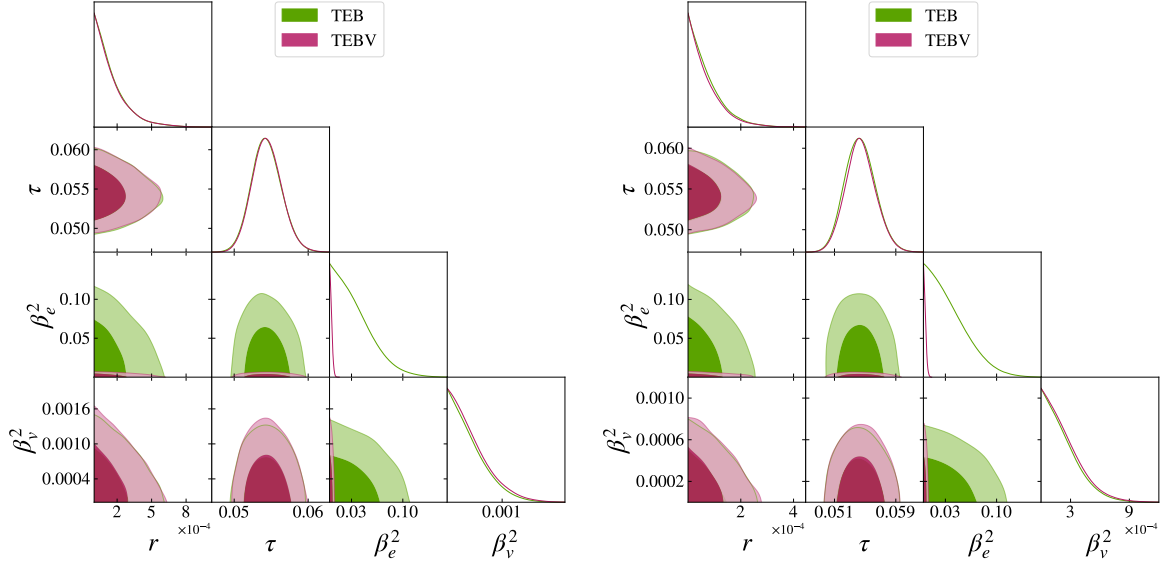
Figure 6. One and two-dimensional posterior probability distributions for LP dataset (see table 2 for details). We report a subset of the total parameter space (ΛCDM model $+ r + \beta_E^2 + \beta_V^2$) showing TTTEEEBB in green and TTTEEEBBVV in magenta. The left panel omits de-lensing procedures ($A_L = 1$), while the right panel employs 70% de-lensing ($A_L = 0.3$).
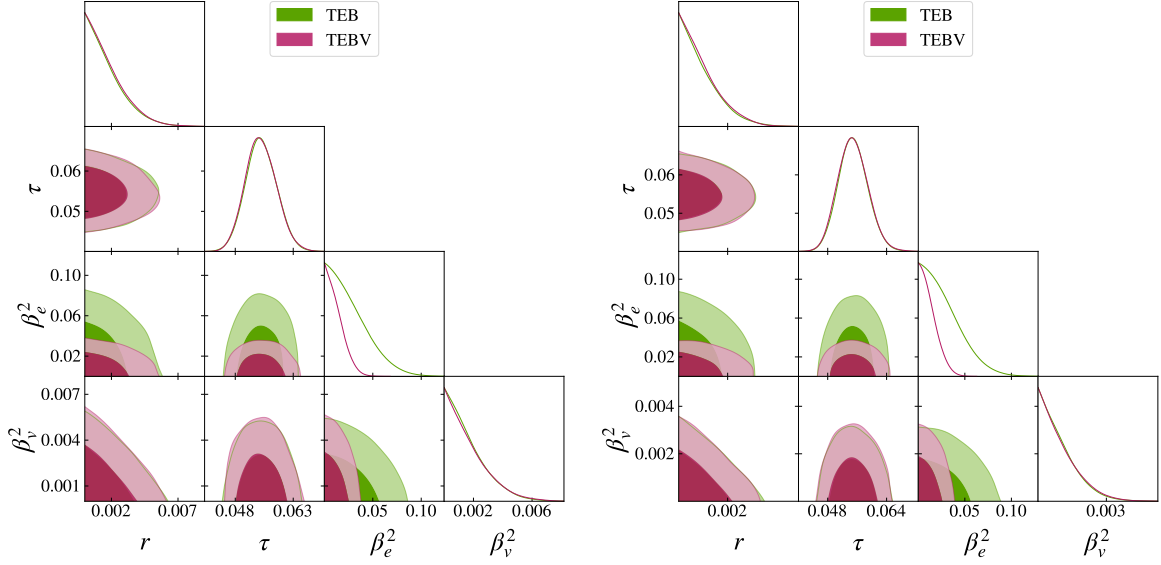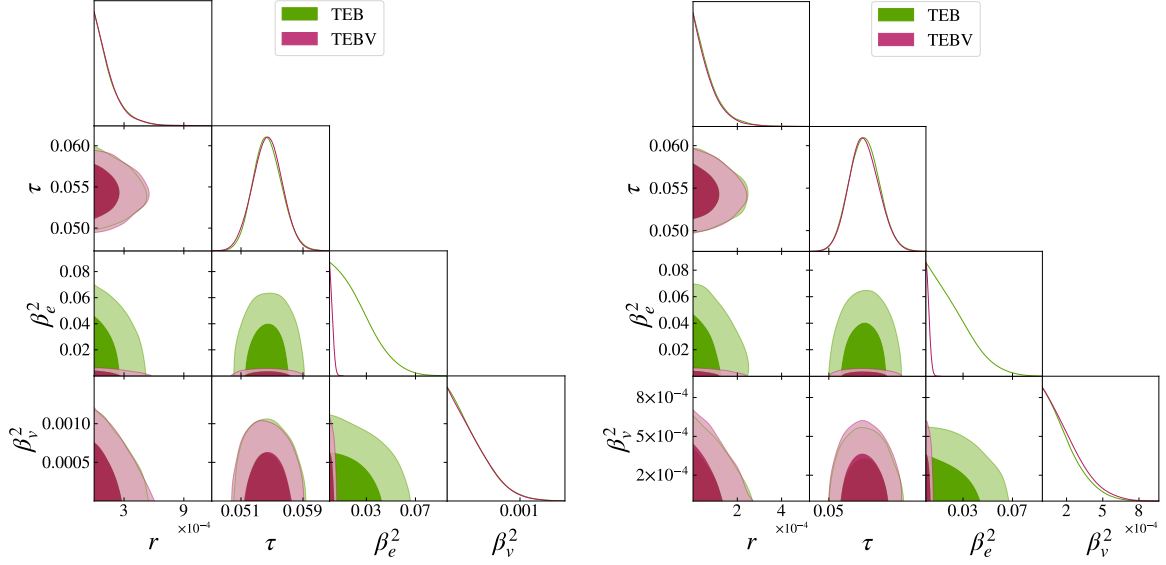
Figure 7. One and two-dimensional posterior probability distributions for *PSO* dataset (see table 2 for details). We report a subset of the total parameter space (ΛCDM model $+ r + \beta_E^2 + \beta_V^2$) showing TTTEEEBB in green and TTTEEEBBVV in magenta. The left panel omits de-lensing procedures ($A_L = 1$), while the right panel employs 70% de-lensing ($A_L = 0.3$).

Figure 8. One and two-dimensional posterior probability distributions for *PS4* dataset (see table 2 for details). We report a subset of the total parameter space (ΛCDM model $+ r + \beta_E^2 + \beta_V^2$) showing TTTEEEBB in green and TTTEEEBBVV in magenta. The left panel omits de-lensing procedures ($A_L = 1$), while the right panel employs 70% de-lensing ($A_L = 0.3$).

Figure 9. One and two-dimensional posterior probability distributions for *LS4* dataset (see table 2 for details). We report a subset of the total parameter space (ΛCDM model $+ r + \beta_E^2 + \beta_V^2$) showing TTTEEEBB in green and TTTEEEBBVV in magenta. The left panel omits de-lensing procedures ($A_{\rm L} = 1$), while the right panel employs 70% de-lensing ($A_{\rm L} = 0.3$).

References

[1] PLANCK collaboration, *Planck 2018 results. VI. Cosmological parameters*, *Astron. Astrophys.* **641** (2020) A6 [*Erratum ibid.* **652** (2021) C4] [arXiv:1807.06209] [INSPIRE].

[2] POLARBEAR collaboration, *A Measurement of the Degree Scale CMB B-mode Angular Power Spectrum with POLARBEAR*, *Astrophys. J.* **897** (2020) 55 [arXiv:1910.02608] [INSPIRE].

[3] POLARBEAR collaboration, *A Measurement of the CMB E-mode Angular Power Spectrum at Subdegree Scales from670 Square Degrees of POLARBEAR Data*, *Astrophys. J.* **904** (2020) 65 [arXiv:2005.06168] [INSPIRE].

[4] ACT collaboration, *The Atacama Cosmology Telescope: DR4 Maps and Cosmological Parameters*, *JCAP* **12** (2020) 047 [arXiv:2007.07288] [INSPIRE].

[5] SPT-3G collaboration, *Measurements of the E-mode polarization and temperature-E-mode correlation of the CMB from SPT-3G 2018 data*, *Phys. Rev. D* **104** (2021) 022003 [arXiv:2101.01684] [INSPIRE].

[6] LiteBIRD collaboration, *Probing Cosmic Inflation with the LiteBIRD Cosmic Microwave Background Polarization Survey*, *PTEP* **2023** (2023) 042F01 [arXiv:2202.02773] [INSPIRE].

[7] SIMONS OBSERVATORY collaboration, *The Simons Observatory: Science goals and forecasts*, *JCAP* **02** (2019) 056 [arXiv:1808.07445] [INSPIRE].

[8] CMB-S4 collaboration, *CMB-S4: Forecasting Constraints on Primordial Gravitational Waves*, *Astrophys. J.* **926** (2022) 54 [arXiv:2008.12619] [INSPIRE].

[9] L. Caloni et al., *Probing Lorentz-violating electrodynamics with CMB polarization*, *JCAP* **03** (2023) 018 [arXiv:2212.04867] [INSPIRE].

[10] G. Choi, C.-T. Chiang and M. LoVerde, *Probing Decoupling in Dark Sectors with the Cosmic Microwave Background*, *JCAP* **06** (2018) 044 [arXiv:1804.10180] [INSPIRE].

[11] I. Dalianis and Y. Watanabe, *Probing the BSM physics with CMB precision cosmology: an application to supersymmetry*, *JHEP* **02** (2018) 118 [arXiv:1801.05736] [INSPIRE].

[12] PRISM collaboration, *PRISM (Polarized Radiation Imaging and Spectroscopy Mission): An Extended White Paper*, *JCAP* **02** (2014) 006 [arXiv:1310.1554] [INSPIRE].

[13] W. Hu and M.J. White, *A CMB polarization primer*, *New Astron.* **2** (1997) 323 [astro-ph/9706147] [INSPIRE].

[14] K. Inomata and M. Kamionkowski, *Circular polarization of the cosmic microwave background from vector and tensor perturbations*, *Phys. Rev. D* **99** (2019) 043501 [arXiv:1811.04957] [INSPIRE].

[15] P. Montero-Camacho and C.M. Hirata, *Exploring circular polarization in the CMB due to conventional sources of cosmic birefringence*, *JCAP* **08** (2018) 040 [arXiv:1803.04505] [INSPIRE].

[16] I. Motie and S.-S. Xue, *Euler-Heisenberg Lagrangian and Photon Circular Polarization*, *EPL* **100** (2012) 17006 [arXiv:1104.3555] [INSPIRE].

[17] R.F. Sawyer, *Photon-photon interactions can be a source of CMB circular polarization*, arXiv:1408.5434 [INSPIRE].

[18] S. Alexander, J. Ochoa and A. Kosowsky, *Generation of Circular Polarization of the Cosmic Microwave Background*, *Phys. Rev. D* **79** (2009) 063524 [arXiv:0810.2355] [INSPIRE].

[19] D. Colladay and V.A. Kostelecky, *Lorentz violating extension of the standard model*, *Phys. Rev. D* **58** (1998) 116002 [hep-ph/9809521] [INSPIRE].

[20] F. Finelli and M. Galaverni, *Rotation of Linear Polarization Plane and Circular Polarization from Cosmological Pseudo-Scalar Fields*, *Phys. Rev. D* **79** (2009) 063002 [arXiv:0802.4210] [INSPIRE].

[21] S. Alexander, E. McDonough, A. Pullen and B. Shapiro, *Physics Beyond The Standard Model with Circular Polarization in the CMB and CMB-21cm Cross-Correlation*, *JCAP* **01** (2020) 032 [arXiv:1911.01418] [INSPIRE].

[22] D. Ejlli, *Magneto-optic effects of the cosmic microwave background*, *Nucl. Phys. B* **935** (2018) 83 [arXiv:1607.02094] [INSPIRE].

[23] D. Ejlli, *On the CMB circular polarization: I. The Cotton-Mouton effect*, *Eur. Phys. J. C* **79** (2019) 231 [arXiv:1810.04947] [INSPIRE].

[24] B.R. Johnson et al., *MAXIPOL: Cosmic Microwave Background Polarimetry Using a Rotating Half-Wave Plate*, *Astrophys. J.* **665** (2007) 42 [astro-ph/0611394] [INSPIRE].

[25] S.A. Bryan, T.E. Montroy and J.E. Ruhl, *Modeling dielectric half-wave plates for cosmic microwave background polarimetry using a Mueller matrix formalism*, *Appl. Opt.* **49** (2010) 6313 [arXiv:1006.3359] [INSPIRE].

[26] ABS collaboration, *Systematic effects from an ambient-temperature, continuously rotating half-wave plate*, *Rev. Sci. Instrum.* **87** (2016) 094503 [arXiv:1601.05901] [INSPIRE].

[27] SPIDER collaboration, *A New Limit on CMB Circular Polarization from SPIDER*, *Astrophys. J.* **844** (2017) 151 [arXiv:1704.00215] [INSPIRE].

[28] M.P. Kennett and D.B. Melrose, *Neutrino emission via the plasma process in a magnetized plasma*, *Phys. Rev. D* **58** (1998) 093011 [astro-ph/9901156] [INSPIRE].

[29] M. Lembo et al., *Cosmic Microwave Background Polarization as a Tool to Constrain the Optical Properties of the Universe*, *Phys. Rev. Lett.* **127** (2021) 011301 [arXiv:2007.08486] [INSPIRE].

[30] R.C. Jones, *A New Calculus for the Treatment of Optical SystemsI. Description and Discussion of the Calculus*, *J. Opt. Soc. Am.* **31** (1941) 488 [INSPIRE].

[31] D. O'Dea, A. Challinor and B.R. Johnson, *Systematic errors in cosmic microwave background polarization measurements*, *Mon. Not. Roy. Astron. Soc.* **376** (2007) 1767 [astro-ph/0610361] [INSPIRE].

[32] S. Giardiello et al., *Detailed study of HWP non-idealities and their impact on future measurements of CMB polarization anisotropies from space*, *Astron. Astrophys.* **658** (2022) A15 [*Erratum ibid.* **671** (2023) C1] [arXiv:2106.08031] [INSPIRE].

[33] W.C. Jones et al., *Instrumental and Analytic Methods for Bolometric Polarimetry*, *Astron. Astrophys.* **470** (2007) 771 [astro-ph/0606606] [INSPIRE].

[34] CLASS collaboration, *Two-year Cosmology Large Angular Scale Surveyor (CLASS) Observations: A First Detection of Atmospheric Circular Polarization at Q Band*, *Astrophys. J.* **889** (2020) 120 [arXiv:1911.01016] [INSPIRE].

[35] I.L. Padilla et al., *Two-year Cosmology Large Angular Scale Surveyor (CLASS) Observations: A Measurement of Circular Polarization at 40 GHz*, arXiv:1911.00391 [DOI:10.3847/1538-4357/ab61f8] [INSPIRE].

[36] G. Pisano et al., *Development and application of metamaterial-based half-wave plates for the NIKA and NIKA2 polarimeters*, *Astron. Astrophys.* **658** (2022) A24 [arXiv:2006.12081] [INSPIRE].

[37] G. Pisano et al., *Achromatic half-wave plate for submillimeter instruments in cosmic microwave background astronomy: experimental characterization*, *Appl. Opt.* **45** (2006) 6982.

[38] G. Savini, G. Pisano and P.A.R. Ade, *Achromatic half-wave plate for submillimeter instruments in cosmic microwave background astronomy: modeling and simulation*, *Appl. Opt.* **45** (2006) 8907.

[39] J.R. Eimer et al., *CLASS Angular Power Spectra and Map-component Analysis for 40 GHz Observations through 2022*, *Astrophys. J.* **963** (2024) 92 [arXiv:2309.00675] [INSPIRE].

[40] R. Mainini et al., *An improved upper limit to the CMB circular polarization at large angular scales*, *JCAP* **08** (2013) 033 [arXiv:1307.6090] [INSPIRE].

[41] D.B. Melrose, *Collective plasma radiation processes*, *Ann. Rev. Astron. Astrophys.* **29** (1991) 31 [INSPIRE].

[42] A. Lewis and S. Bridle, *Cosmological parameters from CMB and other data: A Monte Carlo approach*, *Phys. Rev. D* **66** (2002) 103511 [astro-ph/0205436] [INSPIRE].

[43] K. Abazajian et al., *CMB-S4 Science Case, Reference Design, and Project Plan*, arXiv:1907.04473 [INSPIRE].

[44] LITEBIRD collaboration, *LiteBIRD: JAXA's new strategic L-class mission for all-sky surveys of cosmic microwave background polarization*, *Proc. SPIE Int. Soc. Opt. Eng.* **11443** (2020) 114432F [arXiv:2101.12449] [INSPIRE].

[45] SIMONS OBSERVATORY collaboration, *The Simons Observatory: Astro2020 Decadal Project Whitepaper*, *Bull. Am. Astron. Soc.* **51** (2019) 147 [arXiv:1907.08284] [INSPIRE].

[46] PLANCK collaboration, *Planck 2013 results. I. Overview of products and scientific results*, *Astron. Astrophys.* **571** (2014) A1 [arXiv:1303.5062] [INSPIRE].

[47] M. Gerbino et al., *Likelihood methods for CMB experiments*, *Front. in Phys.* **8** (2020) 15 [arXiv:1909.09375] [INSPIRE].

[48] A. Lewis and A. Challinor, *CAMB: Code for Anisotropies in the Microwave Background*, Astrophysics Source Code Library, record ascl:1102.026, Feb., (2011).

[49] T. Namikawa, *Exact CMB B-mode power spectrum from anisotropic cosmic birefringence*, *Phys. Rev. D* **109** (2024) 123521 [`arXiv:2404.13771`] [InSPIRE].

[50] BICEP and KECK collaborations, *Improved Constraints on Primordial Gravitational Waves using Planck, WMAP, and BICEP/Keck Observations through the 2018 Observing Season*, *Phys. Rev. Lett.* **127** (2021) 151301 [`arXiv:2110.00483`] [InSPIRE].

[51] CMB-S4 collaboration, *CMB-S4: Iterative Internal Delensing and r Constraints*, *Astrophys. J.* **964** (2024) 148 [`arXiv:2310.06729`] [InSPIRE].

[52] K. Wolz et al., *The Simons Observatory: pipeline comparison and validation for large-scale B-modes*, *Astron. Astrophys.* **686** (2024) A16 [`arXiv:2302.04276`] [InSPIRE].

[53] PLANCK collaboration, *Planck 2018 results. V. CMB power spectra and likelihoods*, *Astron. Astrophys.* **641** (2020) A5 [`arXiv:1907.12875`] [InSPIRE].

[54] BICEP2 and KECK ARRAY collaborations, *BICEP2/Keck Array x: Constraints on Primordial Gravitational Waves using Planck, WMAP, and New BICEP2/Keck Observations through the 2015 Season*, *Phys. Rev. Lett.* **121** (2018) 221301 [`arXiv:1810.05216`] [InSPIRE].

[55] S. De and H. Tashiro, *Circular Polarization of the CMB: A probe of the First stars*, *Phys. Rev. D* **92** (2015) 123506 [`arXiv:1401.1371`] [InSPIRE].

[56] N. Lemarchand et al., *Secondary CMB anisotropies from magnetized haloes — I. Power spectra of the Faraday rotation angle and conversion rate*, *Astron. Astrophys.* **630** (2019) A149 [`arXiv:1810.09221`] [InSPIRE].

[57] A. Cooray, A. Melchiorri and J. Silk, *Is the cosmic microwave background circularly polarized?*, *Phys. Lett. B* **554** (2003) 1 [`astro-ph/0205214`] [InSPIRE].

[58] T.-C. Li, T. Zhu, W. Zhao and A. Wang, *Power spectra and circular polarization of primordial gravitational waves with parity and Lorentz violations*, *JCAP* **07** (2024) 005 [`arXiv:2403.05841`] [InSPIRE].

[59] A. Lewis, *GetDist: a Python package for analysing Monte Carlo samples*, `arXiv:1910.13970` [InSPIRE].